NJC

ROYAL SOCIETY OF CHEMISTRY

PAPER

View Article Online
View Journal | View Issue

Cite this: *New J. Chem.*, 2025, **49**, 4849

Hydrodeoxygenation of oleic acid over NiCu bimetallic catalysts supported on Mo-modified niobium phosphate†

Ruiping Wei, * Mingzhu Yao, Ziqi Wang, Huijun Liu, Rongying Xia, Lei Yang, Guanghui Ma, Lijing Gao, Xiaomei Pan and Guomin Xiao

Received 12th November 2024,
Accepted 19th February 2025

DOI: 10.1039/d4nj04885g

rsc.li/njc

The properties of supports have significant effects on the catalytic performance of supported catalysts. The present study involves the synthesis of a series of Mo-modified $NbOPO_4$ supports, which were subsequently utilized for the preparation of supported NiCu bimetallic catalysts *via* a hydrothermal method. The effects of acidity and porosity on the dispersity and valence states of the metal components were systematically investigated *via* BET, XRD, SEM, XPS, NH_3-TPD, and H_2-TPR. The results indicate that the introduction of Mo into the $NbOPO_4$ support enhances the weak acid sites while reducing strong acid sites, thereby preventing excessive acidity from further cracking of long-chain alkanes and reducing carbon deposition on the catalyst surface. Moreover, the synergistic interaction between Ni and Mo leads to the formation of oxygen vacancies and Mo^{5+} sites, as well as alterations in the charge density on the surface of Ni atoms. These factors collectively contribute to the high selectivity of the catalyst toward C18. Catalytic performance of the materials for HDO of oleic acid was assessed and it revealed that NiCu supported on Mo-modified $NbOPO_4$ exhibited significantly enhanced selectivity for C18 compared to those supported on $NbOPO_4$ (53.10% *vs.* 84.16%) under the mild reaction conditions of 250 °C reaction temperature, 3 MPa initial H_2 pressure and 7 h reaction time.

1. Introduction

The increasing concern regarding the depletion of fossil fuels and the urgent need to mitigate environmental pollution are strong drivers for exploring alternative energy sources to fossil-based fuels.[1] The production of diesel-range bio-hydrocarbons from abundant and renewable biomass, using feedstocks such as vegetable oils, waste oils, and lignocellulosic materials, has shown significant potential.[2–4] However, the first-generation biodiesel is limited by its high oxygen content and instability, which has prompted recent research to shift focus towards the second-generation biodiesel. The newer generation consists of oxygen-free alkanes with higher cetane numbers that exhibit enhanced stability and can be blended with petro-diesel in any desired ratio.[5] The hydrodeoxygenation (HDO) process is widely recognized as the most promising method for converting biomass into long-chain alkanes, from the perspectives of green chemistry and industrial application.[6]

The efficiency of green diesel production *via* deoxygenation relies on the metal active sites of the catalyst and the properties of the support. Noble metal catalysts are commonly employed in biomass HDO due to their exceptional hydrogen activation capability at relatively low reaction temperatures, rendering them highly efficient for hydrogenation reactions. Noble metals such as Pd, Pt, Ru, and Rh are widely employed due to their superior hydrogenation performance and efficient activation of hydrogen.[7–10] However, the high cost associated with noble metals restricts their widespread industrial application. Therefore, it is highly desirable to develop novel catalysts that exhibit both low cost and high activity for efficient HDO of oleic acid. Transition metal catalysts, composed of hydrodeoxygenated active metals such as Ni, Co, or Mo and various supports with different acid or base sites, have garnered significant research interest as cost-effective and high-performance alternatives to noble metal catalysts.[11] Recent developments in Ni-based catalysts for HDO of biodiesel have demonstrated significant enhancements in both catalytic activity and selectivity. Zhang *et al.*[12] investigated the catalytic performance of Cu/ZrO_2, Ni/ZrO_2, and $Cu–Ni/ZrO_2$ catalysts in the HDO of oleic acid. The results demonstrated that $Cu–Ni/ZrO_2$ exhibited superior catalytic activity, achieving complete conversion of oleic acid and a yield of *n*-C17 up to 67.8% under conditions of 350 °C and 3 hours. However, catalyst deactivation continues to pose a significant challenge to the broader application of Ni-based catalysts in HDO reactions. For instance, the

School of Chemistry and Chemical Engineering, Southeast University, Nanjing, 211189, P. R. China. E-mail: weiruip@seu.edu.cn

† Electronic supplementary information (ESI) available. See DOI: https://doi.org/10.1039/d4nj04885g

presence of Ni alone will result in undesirable C–C bond cleavage at high temperatures, causing coking and reducing product selectivity and catalyst lifespan.[13] Additionally, deactivation issues such as sintering,[14] coking,[15] and leaching[16] can occur under hydrothermal reaction conditions or in the presence of acidic intermediates. These phenomena significantly impede the catalyst performance. Therefore, in addition to Ni-based catalysts, transition metals such as Cu, Ce, Mo, Co, and Fe[17–21] have been extensively studied for biomass HDO. However, these metals typically require harsh reaction conditions and Cu specifically exhibits low hydrogenation activity under mild conditions, necessitating higher H_2 pressures. Consequently, this study aims to explore an efficient NiCu bimetallic catalyst for the HDO of oleic acid under mild conditions.

The selection of a catalyst support is crucial due to the role of acid sites on the support surface in facilitating the adsorption and activation of reactants at catalytic sites, as well as their significant synergistic effects with metal sites. However, it should be noted that acid sites can easily be quenched by water, which is a byproduct from the HDO reactions.[11] Mesoporous niobium phosphate ($NbOPO_4$), recognized as an efficient solid acid catalyst due to its abundant acid sites with a high Brønsted to Lewis acid ratio and excellent water resistance and thermal stability, has been widely used in various catalytic reactions such as esterification, hydration, dehydration, and oxidation.[22] West *et al.*[23] prepared a niobium-based solid acid-supported Pt bifunctional catalyst and applied it in the dehydration–hydrogenation reaction of sorbitol to produce alkanes at a reaction temperature of 530 K and under a pressure of 54 bar. Fu *et al.*[24] studied the effects of surface defect structures and material distribution of Mn–Ce/$NbOPO_4$-pH*x* (*x* = 2, 7, and 10) catalysts, demonstrating that adjusting the pH value can significantly modify surface defects and species distribution on the support. Their study revealed that a neutral pH facilitates the formation of a porous structure, leading to an increase in the specific surface area and enhanced surface acidity, while also providing excellent resistance to water and sulfur. Additionally, the electron transfer between Nb^{5+} and Mn^{3+} on the support surface generated a substantial number of oxygen vacancies, which contributed to the improved deoxygenation performance of the catalyst.

The present study focuses on the synthesis of NiCu bimetallic catalysts supported on Mo-modified $NbOPO_4$ *via* a hydrothermal method, followed by an evaluation of their HDO performance in converting oleic acid into long-chain alkanes under mild conditions. The primary objective is to achieve high selectivity towards *n*-octadecane (C18) without any carbon loss. Working with Mo modified $NbOPO_4$ supported NiCu bimetallic catalysts, this study revealed that the acidity and porosity of the Mo modified $NbOPO_4$ support could be enhanced to improve the dispersity and stability of the active metal components. This research also aimed to develop efficient, bifunctional, and recyclable solid acid catalysts that address existing challenges and advance sustainable biofuel production by combining the benefits of modified supports and bimetallic synergy under mild reaction conditions.

2. Experimental

2.1 Materials

Nickel nitrate hexahydrate ($Ni(NO_3)_2{\cdot}6H_2O$, 99.0%); copper(II) nitrate trihydrate ($Cu(NO_3)_2{\cdot}3H_2O$, 99.0%); niobium pentoxide (Nb_2O_5, 99.9%); ammonium molybdate tetrahydrate ($(NH_4)_6Mo_7O_{24}{\cdot}4H_2O$, 99.0%); tartaric acid (99.5%); ammonia (37.0%, AR); hydrofluoric acid (AR); diammonium phosphate (99.9%); hexadecyltrimethylammonium bromide (CTAB, AR); oleic acid (AR) and phosphoric acid (AR) were purchased from Sinopharm Chemical Reagent Co. Shanghai, China. Eicosane (GR); octadecane (GR); heptadecane (GR); and *N*-hexane (AR) were purchased from Sigma-Aladdin Corporation (Shanghai, China).

2.2 Preparation of $NbOPO_4$

The $NbOPO_4$ support is prepared *via* a hydrothermal method with tartaric acid niobium as a soft template. Firstly, 0.01 mol of Nb_2O_5 solid was completely dissolved in 20 mL of hydrofluoric acid, after which the resulting solution was transferred into a polytetrafluoroethylene (PTFE)-lined hydrothermal reactor and heated at 100 °C for 7 h. After naturally cooling to room temperature, a clear and transparent solution was obtained. Secondly, an excess of 37% aqueous ammonia was slowly added into the transparent solution to form a $Nb_2O_5{\cdot}nH_2O$ precipitate, which was subsequently filtered, washed to neutrality, and dissolved in 40 mL of tartaric acid solution, followed by heating with stirring at 80 °C for 6 h to produce a niobium tartaric acid solution. Thirdly, the niobium tartaric acid solution was mixed with 2.64 g of ammonium hydrogen phosphate, and the pH of the mixture was adjusted to 2 with phosphoric acid, 26 mL of hexadecyltrimethylammonium bromide (CTAB) aqueous solution was added, and the mixture was stirred vigorously at 40 °C for 1 h before being transferred to a PTFE-lined hydrothermal reactor where it was aged at 160 °C for 24 h. Finally, after cooling naturally, the mixture was filtered and washed, and the resulting solid was dried overnight at 100 °C, then ground and calcined in a muffle furnace at 600 °C for 6 h to obtain the $NbOPO_4$ support.

2.3 Preparation of Mo–$NbOPO_4$

The synthesis of Mo-modified $NbOPO_4$ was similar to that described in Section 2.2, with the molybdenum precursors ($(NH_4)_6Mo_7O_{24}{\cdot}4H_2O$) added in the third step after the pH has been stabilized. Molybdenum precursors in amounts corresponding to 5%, 10%, and 15% (based on the mole ratio of Mo to Nb) were added. Specifically, $(NH_4)6Mo_7O_{24}{\cdot}4H_2O$ was dissolved in the niobium tartaric acid solution to produce materials labeled as *x*Mo–$NbOPO_4$ (*x* = 5%, 10%, and 15%).

2.4 Preparation of NiCu/*x*Mo–$NbOPO_4$ catalysts

Weighed amounts of Ni $(NO_3)_2{\cdot}6H_2O$ and Cu $(NO_3)_2{\cdot}3H_2O$ were dissolved in excess deionized water with continuous stirring until the solution became clear and transparent, which was then used to impregnate various amounts of 5%Mo–$NbOPO_4$, 10%Mo–$NbOPO_4$, and 15%Mo–$NbOPO_4$ supports. The mixtures were impregnated for 12 h, dried overnight at 110 °C, and subsequently calcined in a muffle furnace at 500 °C for 4 h.

The resulting calcined catalyst precursors were placed in porcelain boats and inserted into a tube furnace. The gas-tightness of the tube furnace was ensured, H_2 was introduced into the system at a flow rate of 80–100 mL min^{-1}, followed by increasing the temperature at a rate of 5 °C min^{-1} to reach and maintain it at 550 °C under reduction conditions lasting for 3 h. After natural cooling, the catalysts were removed from the system and labeled as NiCu/5%Mo–$NbOPO_4$, NiCu/10%Mo–$NbOPO_4$, and NiCu/15%Mo–$NbOPO_4$, with equal loadings of Ni and Cu each constituting approximately 10%.

2.5 Catalyst characterization

X-ray diffraction (XRD) patterns of the samples were obtained using a Bruker D8 Advance diffractometer with a Cu Kα (0.1542 nm) X-ray source operating at 40 kV and 40 mA in the range of 2θ from 5 to 85° with a scanning speed of 10 °C min^{-1}.

The specific surface area and pore size of the supports and supported catalysts were evaluated using the BET isotherms of N_2 adsorption at 77 K. Before testing, the supports and supported catalysts were degassed at 120 °C for 14 h and then subjected to adsorption and desorption experiments under 77 K liquid nitrogen.

Acidities of the samples were measured by NH_3 temperature-programmed desorption (NH_3-TPD) using an Auto Chem II 2920 programmed ramp-up adsorption/desorption instrument. The sample was purged with flowing helium at 100 °C for 1 h to remove water vapor and prevent structural changes due to rapid vaporization. The temperature was then increased to 500 °C at a ramping rate of 10 °C min^{-1} and held for 2 h to remove strongly bonded adsorbates and activate the sample. Finally, the sample was purged with helium and cooled to 120 °C.

Hydrogen temperature-programmed reduction (H_2-TPR) was performed using an Auto Chem II 2920 instrument. Typically, 0.05 g of the sample was pre-treated in flowing He for 1 h at 400 °C, followed by cooling to 100 °C. The TPR profiles were recorded from 100 °C to 800 °C at a ramp rate of 10 °C min^{-1}, with a gas flow consisting of a mixture of 10% hydrogen and nitrogen.

Pyridine-FTIR (Py-FTIR) measurements were conducted using a Bruker Tensor 27 spectrometer. After cooling the sample to 50 °C, the background spectrum of the catalyst was collected. Subsequently, pyridine was introduced into the IR cell and adsorbed onto the sample for 20 minutes at 50 °C until saturation was achieved. The temperature was then increased to 150 °C and maintained for 30 minutes to remove weakly adsorbed pyridine under vacuum.

The X-ray photoelectron spectra (XPS) were obtained using the ThermoScientific K-Alpha spectrometer with monochromatic Al Ka radiation (72 W, 12 kV, E = 1486.6 eV).

The surface morphology of the supports was observed under a field-emission scanning electron microscope (SEM, Navo Nano SEM450) with an acceleration voltage of 15 kV.

2.6 Catalytic reaction

The HDO of oleic acid was conducted in a 50 mL mechanical high-pressure reactor. Initially, 2.5 g of oleic acid, 25 g of hexane, and 0.5 g of the catalyst were added into the reactor, which was subsequently purged three times with N_2 to remove any residual air, followed by purging with H_2 three times to eliminate N_2. The desired initial H_2 pressure was introduced at room temperature before heating the reactor to the set reaction temperature while maintaining a stirring speed of 300 rpm for 6 h. Upon completion of the reaction, the reactor was cooled before separating the solid catalyst by centrifugation. The liquid phase products were collected and analyzed using a gas chromatograph equipped with a flame ionization detector (FID) to determine their chemical composition. Separation of the products was achieved using an SE-54 column (30 m × 0.32 mm × 0.50 μm), where the column temperature was initially held at 130 °C for 2 minutes, then increased to 260 °C at a rate of 10 °C min^{-1}, and maintained at 260 °C for 5 minutes while setting both the injector and detector temperatures at 300 °C. *N*-Eicosane was employed as an internal standard for quantitative analysis.

3. Results and discussion

3.1 Catalyst characterization

Fig. 1 shows the XRD patterns of the supports modified with varying amounts of Mo and their corresponding supported NiCu bimetal catalysts. All supports (Fig. 1(a)) exhibit two distinct peaks at 19.8° and 28.4°, which correspond to the crystalline phases of $NbOPO_4$ and Nb_2O_5, respectively, according to standard cards.[25,26] Following the modification of the supports, no diffraction peaks associated with Mo are observed, indicating that Mo is likely highly dispersed within the support. The characteristic peaks of Cu are observed at 43.3° and 50.4° for the NiCu/$NbOPO_4$ catalyst, while the metal Ni peaks (44.5° and 51.8°) exhibit broad and low-intensity diffraction peaks, indicating the presence of relatively small Ni particles. This suggests that the Cu component promotes the dispersion of Ni, highlighting a strong interaction between Ni and Cu.[27] In the case of modified catalysts, as shown in Fig. 1(b), the diffraction peaks of Ni become slightly broader, implying a minor reduction in the crystal size of Ni and better dispersion of Ni atoms due to the promoting effect of the Mo component on Ni.[28] Conversely, for the Cu component, increasing the Mo content leads to more pronounced diffraction peaks, indicating the formation of larger Cu particles.[29] These findings demonstrate the complex interplay between Mo modification and the distribution of metals, which significantly influences their structural properties.

The morphology of the support and crystal structure of metal nanoparticles are critical factors that significantly influence the catalytic performance of the catalyst. Different morphologies expose varying active sites, which can affect the efficiency and selectivity of the catalyst.[30] As illustrated in Fig. 2(a–f), the surface morphology of the $NbOPO_4$ support and its modified versions are highlighted. From Fig. 2(a) and (b), it is evident that the $NbOPO_4$ support consists of numerous layered nanosheets, forming a multi-layered lamellar structure,

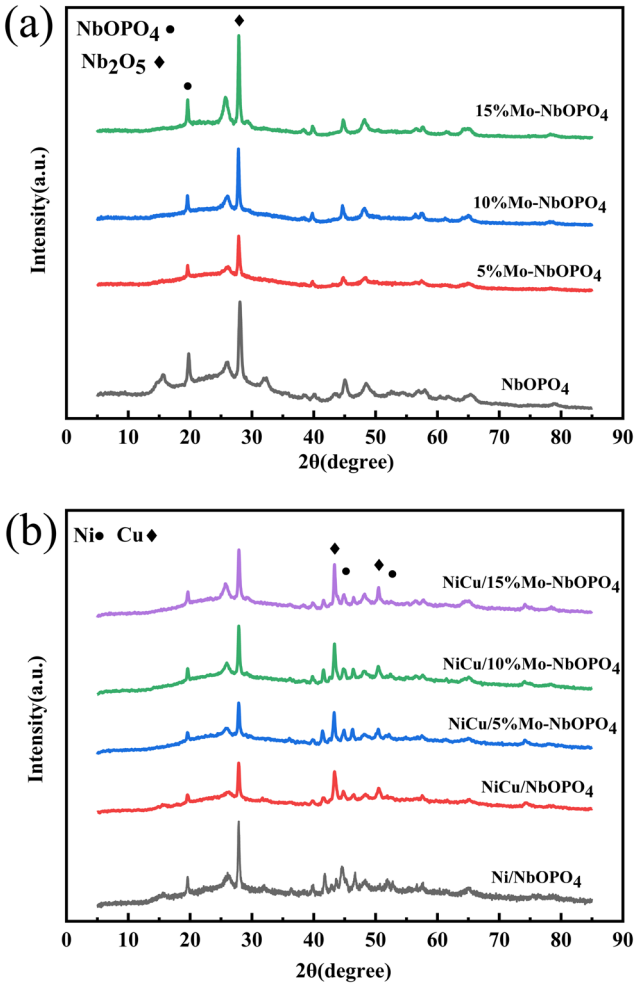

Fig. 1 XRD patterns of (a) supports and (b) reduced catalysts.

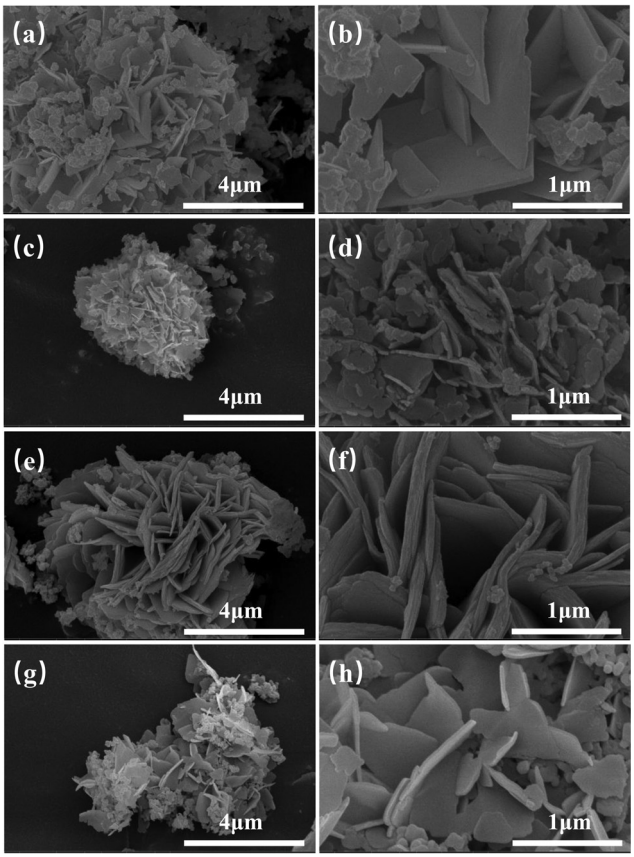

Fig. 2 SEM images of (a) and (b) $NbOPO_4$, (c) and (d) 5%Mo–$NbOPO_4$, (e) and (f) 10%Mo–$NbOPO_4$, and (g) and (h) 15%Mo–$NbOPO_4$.

a distinct morphology resulting from the rapid phosphate-induced precipitation of $NbOPO_4$, leading to formation of lamellar, flower-like clusters. This unique structure provides an extensive surface area that facilitates enhanced mass transfer and increases the frequency of interactions between reactant molecules and active surface centers. In Fig. 2(c–h), the morphology of the Mo-modified $NbOPO_4$ support appears more regular, exhibiting a more distinct flower-like structure likely attributed to Mo doping regulating the lamellar architecture. The extent of Mo doping has a significant impact on both the regularity and stability of the morphology of the support. SEM images (e) and (f) show that doping with 10% Mo achieves a highly regular and robust morphology with probably strengthened interconnections between nanosheets within the support structure. These findings suggest that a higher level of Mo doping contributes to the formation of a stable and well-defined $NbOPO_4$ support structure, thereby enhancing its catalytic properties.

Fig. 3 shows the HADDF-STEM image and EDS line spectra of NiCu/10%Mo–$NbOPO_4$ catalysts. As shown in Fig. 3, Ni and Cu species exhibit varying degrees of aggregation across the supports, while Mo species maintain excellent dispersion, which is in good agreement with the XRD results.

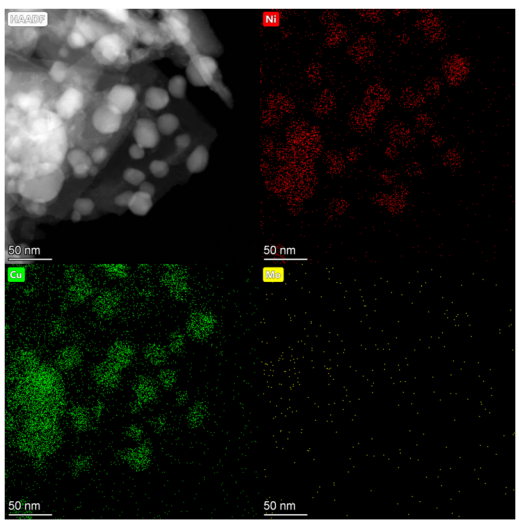

Fig. 3 HAADF-STEM image of NiCu/10%Mo–$NbOPO_4$ and the corresponding EDS.

Fig. 4 shows the N_2 adsorption–desorption isotherms of the supports and reduced catalysts, while their structural properties are summarized in Table 1. According to the IUPAC classification, both the supports (Fig. 4(a)) and catalysts (Fig. 4(b)) exhibit type IV isotherms with H3 and H4-type hysteresis loops, indicating a

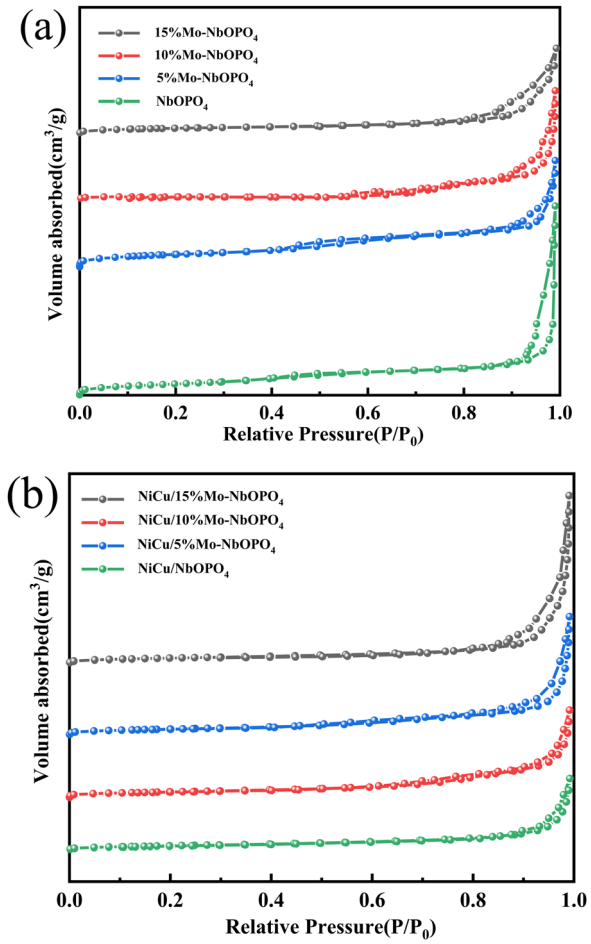

Fig. 4 N_2 adsorption and desorption isotherms of (a) supports and (b) reduced catalysts.

Table 1 Textural properties of supports and reduced catalysts

Sample	Surface area (m^2 g^{-1})	Pore volume (cm^3 g^{-1})	Pore size (nm)
$NbOPO_4$	68.45	0.10	5.93
5%Mo–$NbOPO_4$	60.19	0.19	12.83
10%Mo–$NbOPO_4$	51.64	0.2	15.49
15%Mo–$NbOPO_4$	37.25	0.12	19.48
NiCu/$NbOPO_4$	18.64	0.09	20.83
NiCu/5%Mo–$NbOPO_4$	26.68	0.17	24.99
NiCu/10%Mo–$NbOPO_4$	25.46	0.12	27.15
NiCu/15%Mo–$NbOPO_4$	23.57	0.24	40.82

highly irregular mesoporous structure and confirming the mesoporous nature of the materials. The BET surface area of $NbOPO_4$ is 68.45 m^2 g^{-1}, with a pore size of 5.93 nm. Upon Mo doping modification, the BET surface areas of the supports progressively decrease from 60.19 m^2 g^{-1} to 37.25 m^2 g^{-1} as the Mo content increases. Notably, with 15% Mo doping of the support, the pore size increased from 5.93 nm to 19.48 nm, which is likely due to the structural reorganization or sintering of the support material during the doping process. When incorporating the NiCu bimetallic active sites onto the corresponding supports, consistently reduced BET surface areas are observed compared to those of the supports due to accumulation of metal components on their surfaces. This phenomenon is likely caused by the formation of fine metal oxide particles on the supports blocking some of the pores of the supports during the reduction process.[31] Conversely, the pore sizes of the catalysts are larger than those of the corresponding supports, which can be attributed to pore restructuring and expansion during catalyst formation.

The acidity of the supports and reduced catalysts was measured using NH_3-TPD, with the desorption profiles shown in Fig. 5. Further insights into the acid distribution of the supports and reduced catalysts are provided in Table 2, which shows that the total acidity of $NbOPO_4$ is slightly lower than that of Mo-modified supports indicating relatively similar overall acid contents.

From Fig. 5(a) and Table 2, it can be seen that both $NbOPO_4$ and Mo-modified $NbOPO_4$ supports display three broad peaks, corresponding to the desorption of ammonia on weak (around 110 °C), medium (around 400 °C) and strong (around 625 °C) acid sites. However, all catalysts demonstrate a substantial reduction in acid amounts compared to their corresponding supports, primarily attributed to the interaction between the Ni and Cu metals and the acid sites of the supports.[32] Compared to $NbOPO_4$, the amount of acid sites on Mo-modified supports increases with increasing Mo content. The trend suggests that Mo doping reduces the amount of strong acid sites, likely due

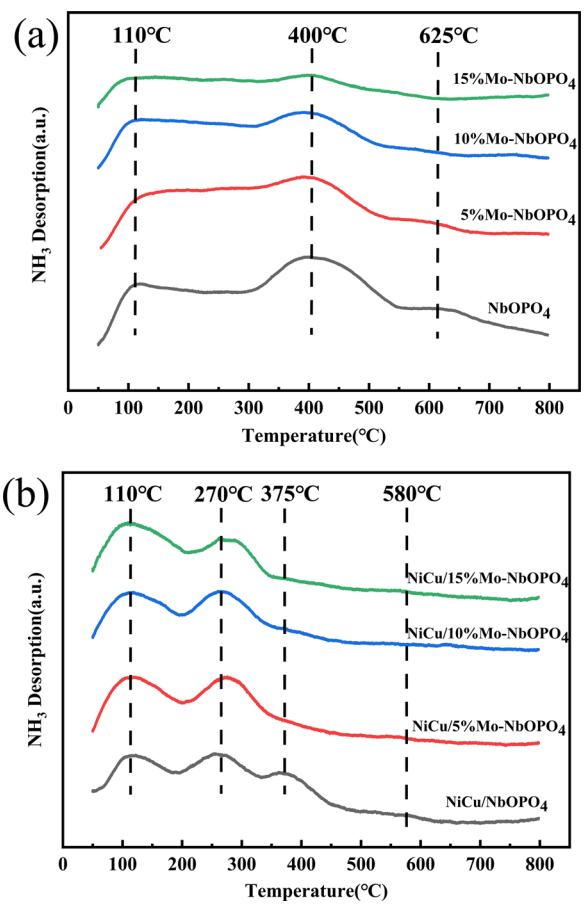

Fig. 5 NH_3-TPD patterns of (a) supports and (b) reduced catalysts.

Table 2 Acidity of the supports and reduced catalysts determined by NH_3-TPD

Sample	Acid sites (mmol g^{-1})			
	Weak ~110 °C	Medium 200–400 °C	Strong ~625 °C	Total
NbOPO4	1.39	1.53	0.13	2.05
5%Mo–NbOPO4	1.67	1.28	0.05	3.00
10%Mo–NbOPO4	1.79	1.38	—	3.17
15%Mo–NbOPO4	1.62	1.24	—	2.86
NiCu/NbOPO4	0.30	0.33	0.05	0.68
NiCu/5%Mo–NbOPO4	0.43	0.36	—	0.79
NiCu/10%Mo–NbOPO4	0.42	0.39	—	0.81
NiCu/15%Mo–NbOPO4	0.42	0.26	—	0.68

to P–OH groups adsorbed onto Mo^{5+} or Mo^{3+}, thereby diminishing strong acid sites on the supports but increasing the weak and total acid sites.[33] As shown in Fig. 5(b), the NH_3 desorption profiles of the corresponding supported catalysts exhibit that there are three peaks (around 110 °C, 270 °C and 375 °C) assigned to three different acid strengths while the strong acid sites around 625 °C disappeared. The NH_3 desorption peak (around 270 °C) for the catalysts compared to their supports suggests the formation of new acidic sites, implying that the acidity of the catalysts is predominantly influenced by the acidity of the metal components of NiCu. It has to be mentioned that excessive acidity of supports and catalysts leads to the further cracking/hydrocracking of long chain hydrocarbons thus enhancing coke deposition on the surface of the catalyst which overall deteriorates the catalyst performance and life time.[34] The reduction in the number of strong acid sites followed by Mo modification could prevent C–C bond cleavage and promote the yield of target products C18, as detailed in Table 4.

The distribution of acid types on the supports and reduced catalysts is shown in Fig. 6, revealing that the synthesized $NbOPO_4$ materials contain both Brønsted (1540 cm^{-1}) and Lewis (1450 cm^{-1}) acid sites. The Brønsted acid sites are primarily derived from P–OH groups and to a lesser extent from Nb–OH sites, while Lewis acid sites are generally

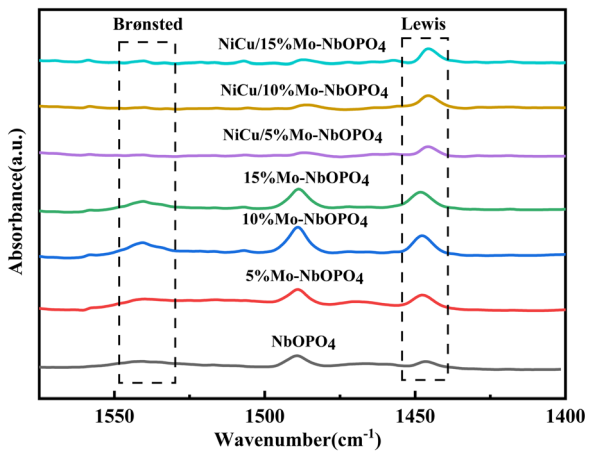

Fig. 6 Pyridine-IR spectra of supports and reduced catalysts.

associated with unsaturated Nb(v) sites.[35] On the Mo-modified supports, a significant increase in both Brønsted and Lewis acid sites is observed, as evidenced by the expanding peak areas for Lewis acid sites and Brønsted acid sites with increasing Mo doping levels. This indicates that the surface doping of Mo on the support effectively enhances the number of active acid sites, thereby altering the acid distribution and potentially influencing the catalytic performance of the supports. Additionally, the supported bimetal catalysts NiCu/*x*Mo–$NbOPO_4$ possess a higher number of Lewis acid sites compared to the series of $NbOPO_4$ supports, leading to enhanced catalytic performance and increased yield of target products C18 as shown in Table 4. This suggests that Lewis acid sites play a beneficial role in preventing C–C bond cleavage and promoting the formation of target product C18.

XPS is used to investigate the chemical states and distribution of Ni, Cu, and Mo species on the reduced catalysts. As shown in Fig. 7(a), the Ni 2p spectra of NiCu/*x*Mo–$NbOPO_4$ display the photoelectron peaks corresponding to Ni^{2+} $2p_{3/2}$ around 856.20 eV. After modification of the $NbOPO_4$ support, the intensity of the Ni^0 $2p_{3/2}$ photoelectron peak increased, possibly owing to the doping of Mo, which induced alterations in the electronic structure of Ni and rendered it less susceptible to oxidation. The presence of lone pairs of electrons in the 3d orbital of Ni atoms, coupled with their high electronegativity, enhances their propensity to interact with the acidic sites on the $NbOPO_4$ support. The Cu^{2+} $2p_{3/2}$ photoelectron peaks, as shown in Fig. 7, exhibit a characteristic that the peak intensity of the binding energy of the Ni^0 $2p_{3/2}$ photoelectron increased, possibly owing to the doping of Mo, which induced alterations in the electronic structure of Ni and rendered it less susceptible to oxidation. The presence of lone pairs of electrons in the 3d orbital of Ni atoms, coupled with their high electronegativity, enhances their propensity to interact with the acidic sites on the $NbOPO_4$ support. The Cu^{2+} $2p_{3/2}$ photoelectron peaks, as shown in Fig. 7(b), exhibit a characteristic binding energy of approximately 934.60 eV, with the highest binding energy observed for NiCu/10%Mo–$NbOPO_4$. This could be attributed to the enhanced interaction between Cu^{2+} and the support, as well as the increased synergistic effect between the bimetallic Ni and Cu species. As depicted in Fig. 7(c), the Mo 3d spectra of the catalysts show three distinct photoelectron peaks corresponding to Mo^{6+}, Mo^{5+} and Mo^{4+} with binding energies approximately at 235.45, 232.62, and 229.75 eV, respectively. Notably, the binding energy of Mo^{6+} $2p_{3/2}$ for NiCu/10%Mo–$NbOPO_4$ is slightly higher than those of NiCu/5%Mo–$NbOPO_4$ and NiCu/15%Mo–$NbOPO_4$ catalysts, which may be due to a stronger chemical bonding between Mo ions and the NiCu bimetallic species leading to an increase of the binding energy.

The distribution of Ni, Cu, and Mo species obtained from the XPS results is presented in Table 3, revealing that the presence of Cu^{2+} indicates the formation of copper compounds with other elements. Notably, NiCu/10%Mo–$NbOPO_4$ and NiCu/5%Mo–$NbOPO_4$ exhibit higher Cu^{2+} concentrations compared to NiCu/15%Mo–$NbOPO_4$, suggesting potential binding between Cu^{2+} and other metal ions, thereby enhancing the

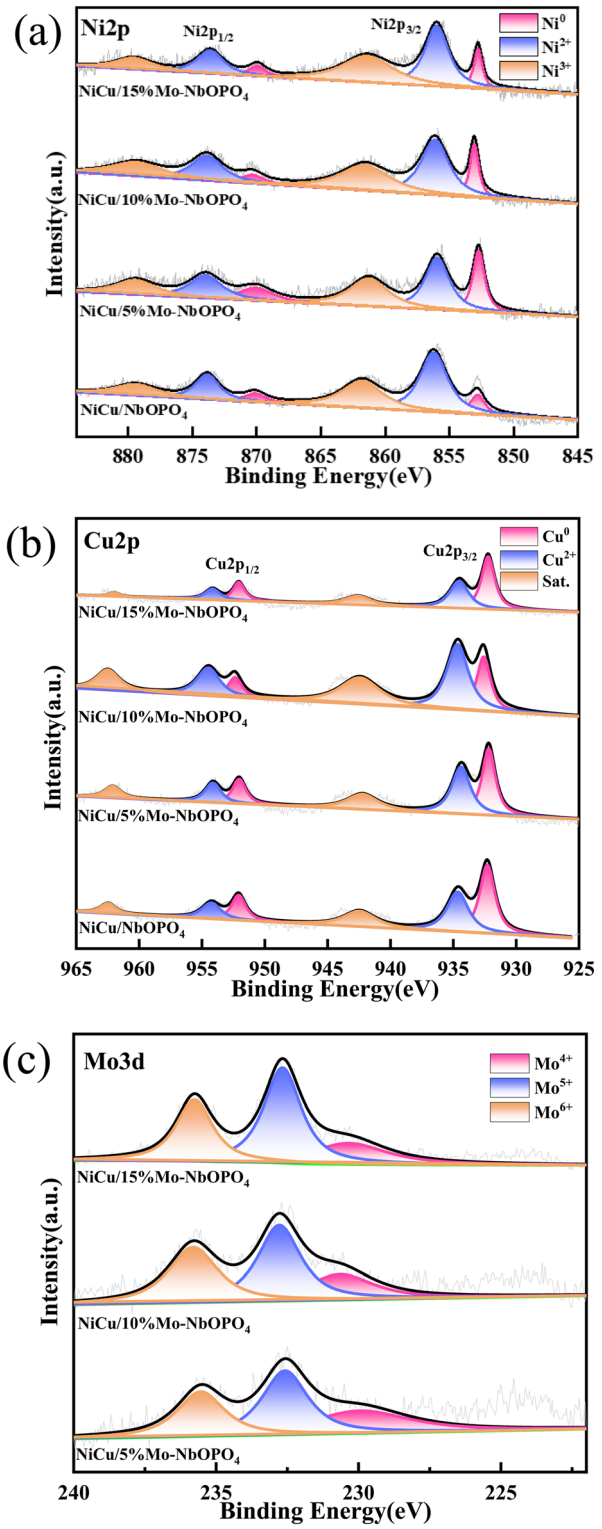

Fig. 7 XPS spectra of (a) Ni 2p, (b) Cu 2p and (c) Mo 3d of reduced catalysts.

synergistic interactions with Ni^{2+} and Mo ions. Consequently, as observed in Table 3, an increase in the Mo content leads to a corresponding decrease in the concentration of Ni^0 on the catalyst surface, indicating that Mo species promote the dispersion of Ni and make it more susceptible to oxidation. Furthermore, the reduction of Mo^{6+} to Mo^{4+} generates corresponding oxygen vacancies which further impact the catalytic properties of the material.[36]

The reduction performance of the calcined catalysts was further investigated using H_2-TPR to study the redox behavior of mixed metal oxides and the interaction between metal Ni and Cu with Mo-modified supports. As shown in Fig. 8(a), the $Ni/NbOPO_4$ catalyst shows a reduction peak around 300 °C and 550 °C, corresponding, respectively, to the reduction of bulk NiO with a weaker interaction with the support and reduction of dispersed NiO, whereas the $Cu/NbOPO_4$ catalyst exhibits a reduction peak around 250 °C, associated with the reduction of CuO interacting with the support.[37]

For the $NiCu/NbOPO_4$ catalyst, the reduction peak around 280 °C can be attributed to the reduction of CuO, NiO and CuO–NiO.[38] Compared to the observed NiO reduction peak for the $Ni/NbOPO_4$ catalyst, it is evident that the presence of Cu^{2+} in the $NiCu/NbOPO_4$ catalyst leads to a shift towards lower temperatures for nickel species, which can be attributed to their incorporation into the structure of NiO. This incorporation alters the chemical state of nickel ions from Ni^{2+} and forms a solid solution with copper ions.[38] The interaction highlights that the addition of Cu species significantly promotes the reduction of NiO.

The reduction peak observed around 650 °C corresponds to the reduction of $NbOPO_4$. In the $NiCu/NbOPO_4$ catalyst, the peak also exhibits a slight shift towards a lower temperature, further supporting the hypothesis that the addition of Cu species facilitates the reduction of $NbOPO_4$. In contrast, the $NiCu/NbOPO_4$ bimetallic catalyst demonstrates distinctly different reduction behavior compared to the $Ni/NbOPO_4$ or $Cu/NbOPO_4$ catalysts. The reduction peaks associated with Ni and Cu species in this bimetallic catalyst show a shift towards lower temperatures, illustrating a strong interaction between them.[27]

For Mo-modified catalysts, the reduction peak observed in the range of 350–500 °C can likely be attributed to the partial reduction of MoO_3 in the high-activity phase, which generates oxygen vacancies and Mo^{5+} sites.[39] It has been suggested that Ni may facilitate the reduction of MoO_3 by hydrogen spill over from Ni to MoO_3.[40–42] This observation aligns with the XPS results shown in Table 3, where the $NiCu/15\%Mo–NbOPO_4$ catalyst exhibits the lowest Ni^0 content and the highest Mo^{6+} content. Consequently, as the Mo content increases, the reduction peak of MoO_3 shifts towards higher temperatures, indicating that a higher content of Mo makes it more difficult for MoO_3 to undergo reduction. Furthermore, with increasing Mo content, the Mo^{6+} content becomes progressively higher, suggesting that Mo likely exists in the form of β-phase $NiMoO_4$,[43] which enhances the interaction between the metal and the support. The results in Table 4 indicate that the $NiCu/10\%Mo–NbOPO_4$ catalyst exhibits the best hydrodeoxygenation performance, consistent with the XPS findings, underscoring the intricate relationship between the Mo content and the catalyst reduction properties while emphasizing the role played by Mo in modulating the redox properties of the system.

Table 3 The distribution of Ni Cu and Mo species on the reduced catalysts

	Distribution of valence state (%)							
	Ni			Cu		Mo		
Catalyst	Ni^0	Ni^{2+}	Ni^{3+}	Cu^0	Cu^{2+}/Cu^+	Mo^{4+}	Mo^{5+}	Mo^{6+}
$NiCu/NbOPO_4$	9.27	54.17	36.56	55.13	44.87	—	—	—
$NiCu/5\%Mo–NbOPO_4$	23.49	41.48	35.04	50.09	49.91	30.89	40.25	28.86
$NiCu/10\%Mo–NbOPO_4$	14.39	47.08	38.54	34.67	65.32	22.29	42.35	35.36
$NiCu/15\%Mo–NbOPO_4$	10.66	46.34	43.01	57.92	42.08	21.81	48.07	38.12

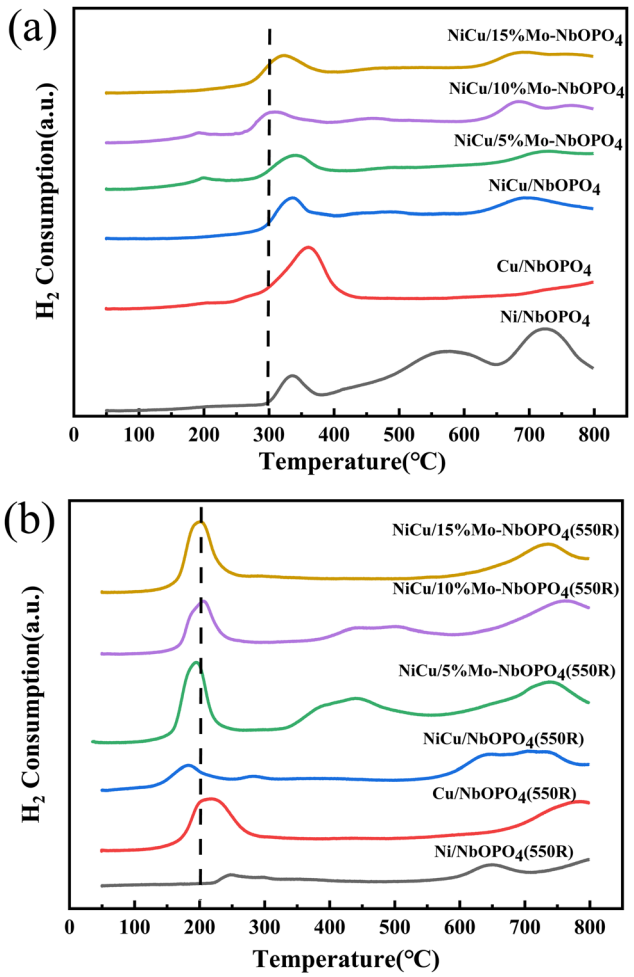

Fig. 8 H_2-TPR profiles of (a) calcined catalysts and (b) reduction catalysts.

3.2 HDO of oleic acid with different catalysts

From the perspective of supports, modifying the composition, morphology, or surface properties of the supports can directly affect the interaction between the supports and metal nanoparticles, subsequently influencing the catalytic performance of the metal.[44] This effect is evident in the modulation of catalytic behavior by support–metal interactions, as demonstrated by the HDO performance of NiCu bimetallic catalysts supported on $NbOPO_4$ with varying Mo loadings shown in Table 4. The conversion of oleic acid consistently remains high across different catalysts, averaging around 99.55%. This can be attributed to the facile hydrogenation of the unsaturated C═C bonds in oleic acid. The introduction of Mo notably enhances selectivity towards C18 products by creating oxygen vacancies (O_v) that act as electron traps, facilitating electron transfer to Ni atoms and resulting in the formation of negatively charged Ni atoms and hydride anions ($H^{\delta-}$).[45] These $H^{\delta-}$ anions play a critical role in hydrogenating polarized C═O bonds and help suppress decarboxylation (C–C bond cleavage), thus favoring the HDO pathway. With 5% Mo loading, the selectivity for C18 increases to 69.04%, suggesting that a moderate amount of Mo effectively promotes C18 formation. As the Mo loading is increased to 10%, the selectivity for C18 is further enhanced to 84.16%, indicating that this amount of Mo optimally enhances catalyst performance by efficiently utilizing $H^{\delta-}$ anions for the HDO pathway. However, the selectivity for C18 declines to 76.23% with 15% loading of Mo, implying that excessive Mo may negatively affect the structure of the support, potentially leading to greater Mo coverage on active metal sites (Ni and Cu) and thereby reducing the availability of these active sites for the desired reaction. This trend reveals that although an initial increase in the Mo loading could enhance the catalytic efficiency and selectivity towards C18, a further increase will hinder the catalytic performance, emphasizing the critical necessity to finely adjust the Mo content. The modification of the $NbOPO_4$ support with Mo significantly influences the catalytic performance of NiCu bimetallic catalysts and optimal Mo loading maximizes the catalytic efficiency by balancing metal–support interactions, underscoring the necessity for precise Mo tuning to achieve optimal catalytic outcomes.

Table 4 The catalytic activities for HDO of oleic acid over Mo-modified catalysts[a]

Catalysts	Conversion (%)	Selectivity (%)	
		Heptadecane	Octadecane
$Ni/NbOPO_4$	99.55	40.11	40.19
$Cu/NbOPO_4$	79.52	4.68	16.53
$NiCu/NbOPO_4$	99.52	39.06	53.10
$NiCu/5\%Mo–NbOPO_4$	99.55	22.05	69.04
$NiCu/10\%Mo–NbOPO_4$	99.55	10.46	84.16
$NiCu/15\%Mo–NbOPO_4$	99.55	18.77	76.23

[a] Reaction conditions: catalyst 0.5 g, oleic acid 2.5 g, reaction time 7 h, reaction temperature 250 °C, and initial H_2 pressure 3.0 MPa.

3.3 Effects of various reaction conditions on HDO of oleic acid

The effects of reaction temperature, pressure, and time on the HDO of oleic acid were investigated over the $NiCu/10\%Mo–NbOPO_4$

catalyst, and the results are presented in Fig. 9. All experiments were conducted under fixed conditions of 2.5 g of oleic acid, 0.5 g of catalyst, and 25 g of *n*-hexane.

As shown in Fig. 9(a), reaction temperature significantly influences the conversion of oleic acid. Within the temperature range of 230 °C to 270 °C, the conversion increased from 81.39% to 99.55% and stabilized at temperatures above 260 °C. Notably, the selectivity of C17 and C18 increased with the increase of temperature and reached their peak at 250 °C. However, upon further increase in temperature to 260 °C, selectivity of C18 declined while selectivity of C17 continued to increase. This can be attributed to excessive temperatures inducing chain cleavage and subsequent hydrogen cracking that reduced C18 selectivity and favored the formation of C17 instead. Therefore, considering both conversion and selectivity factors, 250 °C is identified as the optimal reaction temperature.

The results in Fig. 9(b) demonstrate that reaction pressure primarily affects product selectivity. Oleic acid conversion increases from 75.40% to 99.55% within the initial H_2 pressure range of 2 to 4 MPa, and then levels off at 3 MPa. As the pressure increases, there is a divergence in selectivity trends between C17 and C18, which means that C17 selectivity gradually decreases while C18 selectivity increases. This phenomenon can be attributed the higher hydrogen consumption by the HDO pathway compared to DCO_2 or DCO pathways, making higher H_2 pressures more favorable for enhancing yield of C18 through the HDO route. However, considering safety and energy consumption factors, an initial H_2 pressure of 3 MPa is determined as optimal.

The effect of reaction time on oleic acid conversion is shown in Fig. 9(c). It is indicated that the conversion increases from 72.22% to 99.53% within the time range of 3 to 11 h and is stabilized after 7 h. The selectivity for both C17 and C18 enhanced with increasing reaction time, however, prolonging the reaction beyond 11 h leads to a decline in selectivity for the target products due to excessive reaction and cleavage of the alkane chain. Considering all factors, the optimal reaction conditions to achieve the highest yield of C18 in the HDO of oleic acid using NiCu/10%Mo–$NbOPO_4$ as the catalyst have been identified as a temperature of 250 °C, a hydrogen pressure of 3 MPa H_2, and a reaction time of 7 h.

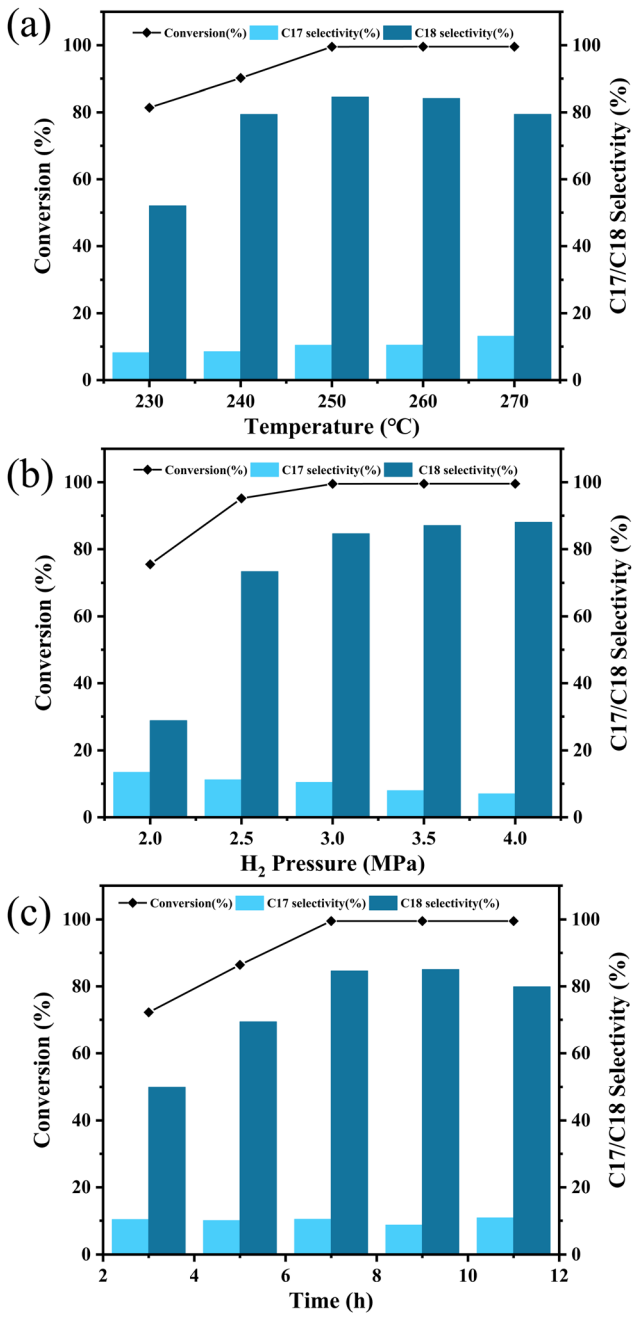

Fig. 9 Effect of (a) reaction temperature (other reaction conditions: catalyst 0.5 g, oleic acid 2.5 g, reaction time 7 h, and initial H_2 pressure 3.0 MPa), (b) initial H_2 pressure (other reaction conditions: catalyst 0.5 g, oleic acid 2.5 g, reaction time 7 h, and reaction temperature 250 °C) and (c) reaction time (other reaction conditions: catalyst 0.5 g, oleic acid 2.5 g, reaction time 7 h, reaction temperature 250 °C, and initial H_2 pressure 3.0 MPa).

3.4 Catalyst stability

The stability of catalysts is a crucial performance indicator that determines its feasibility for industrial applications. Therefore,

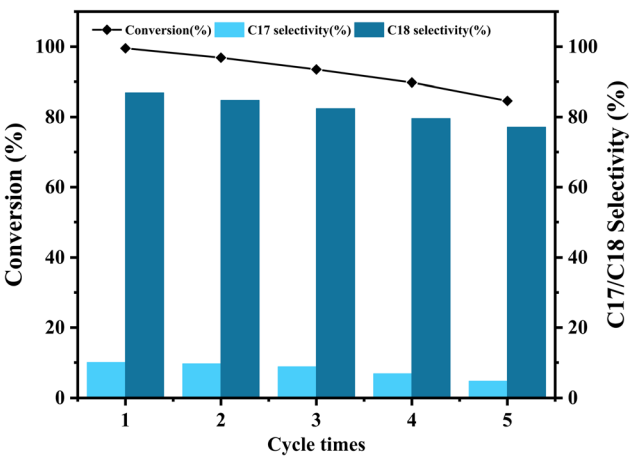

Fig. 10 Recycling performance of NiCu/10%Mo–$NbOPO_4$.

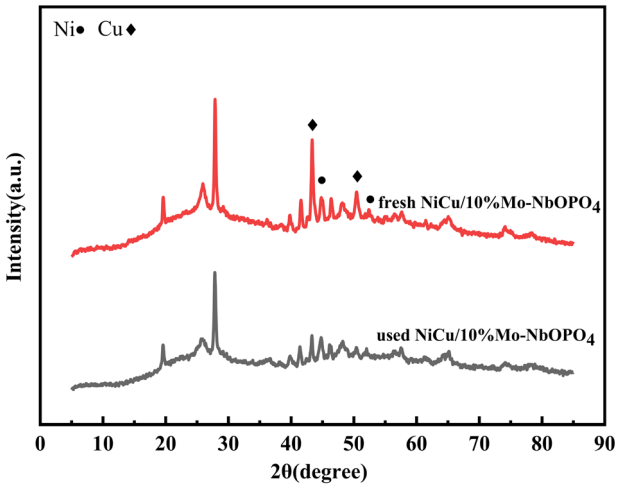

Fig. 11 XRD patterns of fresh NiCu/10%Mo–$NbOPO_4$ and used NiCu/10%Mo–$NbOPO_4$.

the stability was systematically evaluated in this study as depicted in Fig. 10. Following each reaction cycle, the catalyst was recovered by centrifugation and subsequently subjected to drying and calcination to eliminate any adsorbed substances. After undergoing five cycles, the conversion of oleic acid shows a slight decline from 99.53% to 84.60%. Simultaneously, the selectivity of the target product C18 decreased from 86.88% to 78.37%. This reduction in reaction conversion and product selectivity could be attributed to the loss of catalyst powder during the recovery process, suggesting that the catalyst maintains good stability under the optimal conditions.

As shown in Fig. 11, the diffraction peak of Cu slightly weakened, while that of Ni remained unchanged, indicating that during cyclic tests, Cu atoms likely migrated under high temperature and reaction conditions, detaching from aggregates and redistributing on the catalyst surface as smaller particles.

4. Conclusions

A series of Mo-modified $NbOPO_4$ supports were synthesized, loaded with a NiCu bimetal, and subsequently evaluated in the conversion of oleic acid to straight-chain alkanes under mild conditions. This study primarily investigates the role of varying the Mo content in the catalytic efficiency of NiCu bimetallic catalysts for the HDO reaction of oleic acid. The results indicate that the introduction of Mo into the $NbOPO_4$ support enhances its weak acid sites while reducing its strong acid sites, thereby preventing excessive acidity from causing further cracking of long-chain alkanes and increasing surface carbon deposition on the catalyst to promote the selectivity of C18. Compared to NiCu/$NbOPO_4$, the NiCu/10%Mo–$NbOPO_4$ catalyst exhibits a higher density of weak and moderate acid sites, achieving an oleic acid conversion of 99.52% and a C18 selectivity of 84.16%. More importantly, the catalyst maintains good stability during the conversion of oleic acid.

Author contributions

Ruiping Wei: conceptualization, supervision, methodology, writing – review and editing, and project administration. Mingzhu Yao: writing – original draft, visualization, investigation, and formal analysis. Ziqi Wang: investigation and data curation. Huijun Liu: investigation. Rongying Xia: investigation. Lei Yang: investigation. Guanghui Ma: investigation. Lijing Gao: resources, supervision, funding acquisition, and project administration. Xiaomei Pan: resources, supervision, funding acquisition, and project administration. Guomin Xiao: resources, supervision, funding acquisition, methodology, and project administration.

Data availability

The data that support the findings of this study are available upon reasonable request to the corresponding author.

Conflicts of interest

The authors declare no conflicts of interest.

Acknowledgements

The authors acknowledge the financial support from the National Natural Science Foundation of China (No. 2023YFB4203701).

References

1 Y. Guo, Y. Jing, Q. Xia and Y. Wang, *Acc. Chem. Res.*, 2022, **55**, 1301–1312.
2 N. Arun, R. V. Sharma and A. K. Dalai, *Renewable Sustainable Energy Rev.*, 2015, **48**, 240–255.
3 T. K. Hari, Z. Yaakob and N. N. Binitha, *Renewable Sustainable Energy Rev.*, 2015, **42**, 1234–1244.
4 J. Justicia, J. A. Baeza, L. Calvo, F. Heras and M. A. Gilarranz, *Chem. Eng. J.*, 2023, **477**, 146860.
5 J. Zhong, J. Pérez-Ramírez and N. Yan, *Green Chem.*, 2021, **23**, 18–36.
6 I. V. Shamanaev, E. Y. Gerasimov, V. P. Pakharukova and G. A. Bukhtiyarova, *React. Kinet., Mech. Catal.*, 2024, **137**, 935–949.
7 I. H. Choi, K. R. Hwang, J. S. Han, K. H. Lee, J. S. Yun and J. S. Lee, *Fuel*, 2015, **158**, 98–104.
8 C. Ju, Y. Zhou, M. He, Q. Wu and Y. Fang, *Renewable Energy*, 2016, **97**, 1–7.
9 H. Wang, H. Ruan, H. Pei, H. Wang, X. Chen, M. P. Tucker, J. R. Cort and B. Yang, *Green Chem.*, 2015, **17**, 5131–5135.
10 Y. He, R. Liu, D. Yellezuome, W. Peng and M. Tabatabaei, *Renewable Energy*, 2022, **184**, 487–497.
11 L. Chen, G. Li, M. Zhang, D. Wang, S. Lia, C. Zhang, X. Lia and K. H. Chung, *Fuel*, 2020, **282**, 118842.
12 Z. Zhang, H. Chen, C. Wang, K. Chen, X. Lu, P. Ouyang and J. Fu, *Fuel*, 2018, **230**, 211–217.
13 W. Li, Y. Gao, S. Yao, D. Ma and N. Yan, *Green Chem.*, 2015, **17**, 4198–4205.

14 N. Karanwal, M. G. Sibi, M. K. Khan, A. A. Myint, B. C. Ryu, J. W. Kang and J. Kim, *ACS Catal.*, 2021, **11**, 2846–2864.
15 K. L. MacIntosh and S. K. Beaumont, *Top. Catal.*, 2020, **63**, 1446–1462.
16 H. Singh, N. Iyengar, P. Rajpu and A. K. Sinha, *Mater. Res. Bull.*, 2019, **112**, 363–375.
17 V. Torres-Bujalance, C. A. Prieto, K. E. Rodriguez Espinoza and L. A. González-Mendoza, *Energy Fuels*, 2024, **38**, 4312–4324.
18 K. Zhang, X. Liu, J. Bi, A. BaQais, B. B. Xu, M. A. Amin, Y. Hou, X. Liu, H. Li, H. Algadi, J. Xu and Z. Guo, *New J. Chem.*, 2023, **47**, 18272–18284.
19 B. S. Shrirame and S. K. Maity, *Catal. Today*, 2024, **442**, 114917.
20 S. Feng, H. Zhou, Z. Wang, S. Shu, X. Zhang and J. Chen, *New J. Chem.*, 2024, **48**, 6919–6932.
21 X. Cao, J. Zhao, S. Jia, F. Long, Y. Chen, X. Zhang, J. Xu and J. Jiang, *Chem. Eng. J.*, 2024, **481**, 148345.
22 S. Kang, R. Miao, J. Guo and J. Fu, *Catal. Today*, 2021, **374**, 61–76.
23 R. M. West, M. H. Tucker, D. J. Braden and J. A. Dumesic, *Catal. Commun.*, 2009, **10**, 1743–1748.
24 S. Fu, Q. Qin, J. Li, B. Chu, J. Zhu, D. Mo, J. Wang, L. Dong and B. Li, *J. Alloys Compd.*, 2023, **942**, 168836.
25 Y. Zhang, J. Wang, J. Ren, X. Liu, X. Li, Y. Xia, G. Lu and Y. Wang, *Catal. Sci. Technol.*, 2012, **2**, 2485–2491.
26 P. Sun, X. Long, H. He, C. Xia and F. Li, *ChemSusChem*, 2013, **6**, 2190–2196.
27 X. Cao, F. Long, F. Wang, J. Zhao, J. Xu and J. Jiang, *Renewable Energy*, 2021, **180**, 1–13.
28 O. Kikhtyanin, A. Smirnov, V. Korolova, I. Paterová and D. Kubička, *Appl. Catal., A*, 2024, **685**, 119889.
29 X. Cao, F. Long, Q. Zhai, P. Liu, J. Xu and J. Jiang, *Renewable Energy*, 2020, **162**, 2113–2125.
30 T. W. van Deelen, C. Hernández Mejía and K. P. de Jong, *Nat. Catal.*, 2019, **2**, 955–970.
31 S. V. Sancheti, G. D. Yadav and P. K. Ghosh, *ACS Omega*, 2020, **5**, 5061–5071.
32 T. Jiang, Q. Zhang, T. J. Wang, Q. Zhang and L. L. Ma, *Energy Convers. Manage.*, 2012, **59**, 58–65.
33 N. Chen, S. Gong and E. W. Qian, *Appl. Catal., B*, 2015, **174–175**, 253–263.
34 A. A. Dabbawala, O. Elmutasim and M. A. Baker, *et al.*, *Appl. Surf. Sci.*, 2023, **640**, 158294.
35 P. Carniti, A. Gervasini, F. Bossola and V. Dal Santo, *Appl. Catal., B*, 2016, **193**, 93–102.
36 R. Wei, L. Zhang, M. Tian, Z. Cai, Z. Shao, L. Gao, J. Zhang, X. Guo and G. Xiao, *New J. Chem.*, 2023, **47**, 3000–3008.
37 B. Mile, D. Stirling, M. A. Zammitt, A. Lovell and M. Webb, *J. Catal.*, 1988, **114**, 217–229.
38 A. V. Fedorov, R. G. Kukushkin, P. M. Yeletsky, O. A. Bulavchenko, Y. A. Chesalov and V. A. Yakovlev, *J. Alloys Compd.*, 2020, **844**, 156135.
39 C. Dupont, R. Lemeur, A. Daudin and P. Raybaud, *J. Catal.*, 2011, **279**, 276–286.
40 M. A. Tsurov, P. V. Afanasiev and V. V. Lunin, *Appl. Catal., A*, 1993, **105**, 205–221.
41 H. M. Abdel-Dayem, *Ind. Eng. Chem. Res.*, 2007, **46**, 2466–2472.
42 J. L. Brito, J. Laine and K. C. Pratt, *J. Mater. Sci.*, 1989, **24**, 425–431.
43 H. Liu, C. Yin, X. Li, Y. Chai, Y. Li and C. Liu, *Catal. Today*, 2017, **282**, 222–229.
44 T. W. van Deelen, C. Hernández Mejía and K. P. de Jong, *Nat. Catal.*, 2019, **2**, 955–970.
45 H.-Y. T. Chen, S. Tosoni and G. Pacchioni, *ACS Catal.*, 2015, **5**, 5486–5495.